Journal of Materials Chemistry C

Lattice matched GeSn/InAlAs heterostructure: Role of Sn in energy band alignment, atomic layer diffusion and photoluminescence

Journal:	*Journal of Materials Chemistry C*
Manuscript ID	TC-ART-03-2023-001018.R1
Article Type:	Paper
Date Submitted by the Author:	12-Jun-2023
Complete List of Authors:	Karthikeyan, Sengunthar; Virginia Tech, Bradley Department of Electrical and Computer Engineering Joshi, Rutwik; Virginia Tech, Bradley Department of Electrical and Computer Engineering Zhao, Jing; Virginia Tech, Department of Geosciences Bodnar, Robert; Virginia Tech, Department of Geosciences Magill, Brenden; Virginia Tech, Pleimling, Yannick; Virginia Tech, Department of Physics Khodaparast, Giti; Virginia Tech, Department of Physics Hudait, Mantu; Virginia Tech, Electrical and Computer Engineering

Journal of Materials Chemistry C

ARTICLE

Lattice matched GeSn/InAlAs heterostructure: Role of Sn in energy band alignment, atomic layer diffusion and photoluminescence

Received 22nd Mar. 2023,
Accepted xxth xx 2023

DOI: 10.1039/x0xx00000x

www.rsc.org/

Sengunthar Karthikeyan[a], Rutwik Joshi[a], Jing Zhao[b], Robert J. Bodnar[b], Brenden A. Magill[c], Yannick Pleimling[c], Giti A. Khodaparast[c] and Mantu K. Hudait*[a]

Abstract

Germanium alloyed with α-tin (GeSn) transitions to a direct bandgap semiconductor of significance for optoelectronics. It is essential to localize the carriers within the active region for improving the quantum efficiency in a GeSn based laser. In this work, epitaxial GeSn heterostructure material systems were analyzed to determine the band offsets for carrier confinement: (i) a 0.53% compressively strained $Ge_{0.97}Sn_{0.03}$/AlAs; (ii) a 0.81% compressively strained $Ge_{0.94}Sn_{0.06}$/Ge; and (iii) a lattice matched $Ge_{0.94}Sn_{0.06}/In_{0.12}Al_{0.88}As$. The phonon modes in GeSn alloys were studied using Raman spectroscopy as a function of Sn composition, that showed Sn induced red shifts in wavenumbers of the Ge–Ge longitudinal optical phonon mode peaks. The material parameter *b* representing strain contribution to Raman shifts of a $Ge_{0.94}Sn_{0.06}$ alloy was determined as $b = 314.81 \pm 14$ cm^{-1}. Low temperature photoluminescence measurements were performed at 79 K to determine direct and indirect energy bandgaps of $E_{g,\Gamma} = 0.72$ eV and $E_{g,L} = 0.66$ eV for 0.81% compressively strained $Ge_{0.94}Sn_{0.06}$, and $E_{g,\Gamma} = 0.73$ eV and $E_{g,L} = 0.68$ eV for lattice matched $Ge_{0.94}Sn_{0.06}$ epilayers. Chemical effects of Sn atomic species were analyzed using x-ray photoelectron spectroscopy (XPS), revealing a shift in Ge 3d core level (CL) spectra towards the lower binding energy affecting the bonding environment. Large valence band offset of $\Delta E_V = 0.91 \pm 0.1$ eV and conduction band offset of $\Delta E_{C,\Gamma-X} = 0.64 \pm 0.1$ eV were determined from the $Ge_{0.94}Sn_{0.06}/In_{0.12}Al_{0.88}As$ heterostructure using CL spectra by XPS measurements. The evaluated band offset was found to be of type–I configuration, needed for carrier confinement in a laser. In addition, these band offset values were compared with the first-principles-based calculated Ge/InAlAs band alignment, and it was found to have arsenic up-diffusion limited to 1 monolayer of epitaxial GeSn overlayer, ruling out the possibility of defects induced modification of band alignment. Furthermore, this lattice matched GeSn/InAlAs heterostructure band offset values were significantly higher than GeSn grown on group IV buffer/substrates. Therefore, a lattice matched GeSn/InAlAs material system has large band offsets offering superior carrier confinement to realize a highly efficient GeSn based photonic device.

Introduction

Advent of on-chip optoelectronic system integration with silicon (Si) platforms led to extensive research on group IV (*i.e.,* SiGeSn, GeSn, Ge) based materials for lasers and photodetectors.[1–12] Germanium (Ge) is a popular choice due to its optoelectronic functionalities and pseudo direct bandgap nature, where the differences in indirect to direct bandgap energy (E_g) is limited to $E_{g,\Gamma} - E_{g,L} = \sim 0.136$ eV,[13] at room temperature. The indirect to direct bandgap transition of Ge is attainable either through strain engineering[14, 15] or by alloying with α-tin (Sn).[1–12] However, strain engineering is limited by the critical layer thickness (h_c) of the active region,

[a] Advanced Devices & Sustainable Energy Laboratory (ADSEL), Bradley Department of Electrical and Computer Engineering, Virginia Tech, Blacksburg, Virginia 24061, USA. E-mail: mantu.hudait@vt.edu; Mob.:540-231-6663.
[b] Fluids Research Laboratory, Department of Geosciences, Virginia Tech, Blacksburg, Virginia 24061, USA.
[c] Department of Physics, Virginia Tech, Blacksburg, Virginia, 24061, USA.

beyond which defects and misfit dislocations (MDs)[16–20] are introduced due to strain relaxation, which in turn will decrease the carrier lifetime due to its sensitivity to defects and dislocations, and will increase the junction leakage current in a photodetector or a laser. However, growing a $Ge_{1-y}Sn_y$ alloy as a lattice matched epitaxial layer with an underlying metamorphic buffer like $In_xAl_{1-x}As$ or $In_xGa_{1-x}As$ turns GeSn into a tunable (by varying Sn composition) direct bandgap material with no strain/defect-limited thickness constraints and also preserving the orderly arrangement of the crystal lattice. In addition, alloying epitaxial Ge with Sn lowers the conduction band minima (CBM) at the Γ–valley faster than the *L*–valley, where the indirect to direct bandgap crossover could occur at approximately 6–8% Sn.[1–12] Composition of Sn for this transition is stated over a range, since the bowing parameter of $Ge_{1-y}Sn_y$ in the computation of energy bandgap varies between experimental and first-principles calculations.[21] Additionally, $Ge_{1-y}Sn_y$ material has inherent advantages, such as: (i) increased direct band transitions of the carriers between conduction and valence bands, improving optical absorption to provide high photodetector responsivities;[22–24] (ii) lower effective mass (m_{eff}) of carriers in the Γ–valley than *L*–valley enhances mobility – thereby boosting the ON-current in a low power transistor;[25, 26] (iii) compatibility with Si CMOS technology;[27–30] (iv) high carrier lifetime due to reduced surface roughness[31] by mitigating surface states induced recombination. Hence, a virtually defect-free lattice matched GeSn/InAlAs (or InGaAs) heterostructure is necessary to make better use of $Ge_{1-y}Sn_y$ material in photonic integrated circuits (PICs) and optoelectronic applications.

For optical functionalities, localizing carriers in the active region is a requisite for direct transitions. However, carrier confinement in a GeSn active region that is synthesized on small bandgap materials like Si, Ge, SiGe, or SiGeSn is poor due to: (i) small conduction band (ΔE_C) and valence band–offsets (ΔE_V)[32] that reduce the electrical and optical confinements (*i.e.*, minimal difference in the refractive indices of these materials with GeSn) of the photogenerated carriers in a photodetector (*i.e.*, decreasing the quantum efficiency) and the injected carriers in a laser (*i.e.*, increasing the threshold current density);[33] (ii) the number of interatomic diffusion layers can impactfully alter the band alignment[34] with little tolerance for error in the heterostructures with small band offsets; and (iii) the lattice mismatch between the GeSn and the small bandgap materials creates defects when the active region is grown beyond the critical layer thickness, reducing the crystal lattice coherency that affects the material quality and degrades the carrier lifetime due to increase in non-radiative recombination centers.[35,36] However, a GeSn alloy grown on a lattice matched, large bandgap material such as InAlAs or InGaAs is a central route to synthesize a device quality material with excellent arrangement of the crystal lattice. The optical device performance parameters are improved by large band offsets, such as in a: (i) photodetector – reduced junction leakage, reduce carrier recombination at the interface, improved back reflection and hence overall quantum efficiency; (ii) laser – reduced leakage, high gain, high injection efficiency and increased operating temperature. A lattice matched GeSn/InAlAs heterostructure has been previously demonstrated with good quality.[31] Note that InAlAs has a larger bandgap than InGaAs and also reduces interatomic diffusion due to a stronger Al–As bond than Ga–As bond.[34] At the isovalent heterojunctions like GeSn on Si, Ge, SiGe, or SiGeSn, study of the chemical stoichiometry in the bulk or epitaxial regions is sufficient to line up the energy bands. However, at the heterovalent junctions like GeSn on InAlAs, studied in this work, determining the band offsets necessitates *ab-initio* calculations of the band alignment at the heterointerface. Therefore, to experimentally determine the band alignment at the heterovalent junctions, twofold study covering the interfacial chemical bond and bonding in the bulk/epitaxial regions is essential.[34, 37] The chemical bonding at an heterovalent interface can strikingly alter the band offsets from type–I (straddling) to type–II (staggered).[34,39] Likewise, defects at an interface can also effectively change the band offsets and subsequently the band alignment from type–II (staggered) to type–III (broken gap).[40] Hence, all the three aspects of large band offsets, low interfacial defects and reduced interatomic diffusion are crucial to maintain the type-I band alignment for optoelectronic applications.

In this work, band lineup at the lattice matched GeSn/InAlAs heterointerface is experimentally determined as type–I, a preferred choice in optical devices.[41, 42] Nature of energy band alignment at the $Ge_{0.94}Sn_{0.06}/In_{0.12}Al_{0.88}As$ heterojunction is studied by probing the chemical bonding properties in the epitaxial and interfacial regions using x-ray photoelectron spectroscopy (XPS). Consequently, effect of the Sn atomic species on the binding energy distribution curves (EDCs) of Ge (in the substitutional GeSn alloy) is investigated. The chemical shift in the binding energy (BE) of Ge 3d core level (CL) states due to Ge–Sn bond is probed for three different GeSn/III-V heterostructure material systems. Such a shift makes the heterointerfacial bonding different and changes the band offsets in the lattice matched $Ge_{0.94}Sn_{0.06}/In_{0.12}Al_{0.88}As$ material system. ΔE_V is measured using the binding energies of CL states of the atomic elements present in the active region (GeSn) and the underlying InAlAs buffer layer.

ΔE_C is deduced from three parameters, namely: measured ΔE_V, bandgap of $Ge_{0.94}Sn_{0.06}$ and bandgap of $In_{0.12}Al_{0.88}As$. This experiment brings forth the nature of band alignment at the $Ge_{0.94}Sn_{0.06}/In_{0.12}Al_{0.88}As$ heterointerface as type–I (straddling), with both ΔE_V and ΔE_C large enough at room temperature to superiorly confine the electrons and holes within the optically active epitaxial $Ge_{0.94}Sn_{0.06}$ region. Additionally, this material system is also highly resistant to defect assisted and interatomic diffusion assisted alteration to the type of band alignment. Moreover, the Raman spectroscopy measurements studying the vibrational properties of GeSn alloys showed red shifts in longitudinal optical (LO) phonon peak wavenumbers for the lattice matched $Ge_{0.94}Sn_{0.06}$ epilayer with respect to the 0.81% compressively strained $Ge_{0.94}Sn_{0.06}$ epilayer, confirming less phonon mediated optical transitions to *L*–valley in the former. In addition, low temperature (79 K) photoluminescence (PL) analysis of GeSn alloys with 6% Sn showed much more reduced separation between the *L*- and Γ- valleys in lattice matched $Ge_{0.94}Sn_{0.06}/In_{0.12}Al_{0.88}As$ system versus the compressively strained $Ge_{0.94}Sn_{0.06}$/Ge system. Hence, the lattice matched $Ge_{0.94}Sn_{0.06}/In_{0.12}Al_{0.88}As$ heterostructure, that highly localizes the carrier within the active region, extends itself as an appropriate candidate for group IV GeSn based optoelectronic applications.

Experiment

Epitaxial GeSn layers were grown by dual chamber solid source molecular beam epitaxy (MBE) system on (100)/2° semi-insulating GaAs substrates. The interconnected growth chambers, of group IV and III-V, are isolated using an ultra-high-vacuum transfer chamber to avoid the interdiffusion among them. **Fig. 1** shows the schematics of each layer structure studied in this work. XPS analysis of *sample A* with a 270 nm thick Ge epilayer grown on a 170 nm AlAs buffer layer in the same MBE system[43] as *samples B, C* and *D* is taken as a reference to analyze the chemical bonding properties of Ge in GeSn epitaxial layers of different thicknesses: (i) *sample B* – 350 nm pseudomorphic $Ge_{0.97}Sn_{0.03}$ epitaxial layer grown on 250 nm AlAs buffer; (ii) *sample C* – 50 nm pseudomorphic $Ge_{0.94}Sn_{0.06}$ epitaxial layer grown on 50 nm Ge buffer; and (iii) *sample D* – 350 nm lattice matched $Ge_{0.94}Sn_{0.06}$ epitaxial layer grown on 500 nm $In_{0.12}Al_{0.88}As$ buffer layer of constant composition. All the samples are unintentionally doped of *n-type* to the order of 10^{18} cm^{-3}. The material synthesis, compositional and structural analysis of these heterostructure materials systems are discussed elsewhere.[31] Wherein it was shown using high-resolution x-ray diffraction that the GeSn epitaxial layers were of coherent crystalline quality, and the lattice matched *sample D* had a narrower reciprocal lattice point contour than the compressively strained *samples* B (~0.53% strain) and *C* (~ 0.81% strain), conforming to the need of growing a lattice matched GeSn epitaxial layer. Also characterized were the effective carrier lifetimes of the GeSn epitaxial layers using microwave reflection photoconductive decay technique (μ-PCD) probed at 300 K to extract carrier lifetimes of 220 ns, 468 ns and 324 ns for *samples B*, *C* and *D*, respectively.[31] These material characterization techniques showed the superior quality of the epitaxial GeSn layers.

In this work, to begin with analyzing the physical effects of Sn atom on Ge atom in a GeSn alloy, Raman spectroscopy measurements were performed at room temperature. The vibrational properties of the epitaxial $Ge_{1-y}Sn_y$ layers in *samples A–D* were captured in a backscattering geometry using JY Horiba LabRam HR800-UV system, equipped with an Ar^+ laser source operating at 514.48 nm wavelength. The power of the laser source at input was ~ 65 mW and the laser beam

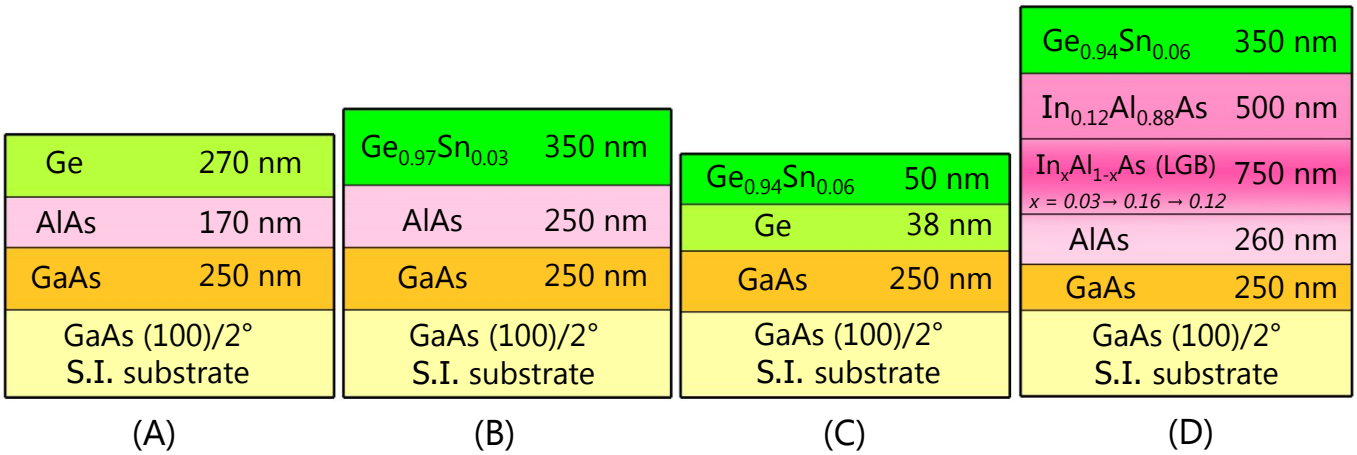

Fig. 1: Cross-sectional schematics of $Ge_{1-y}Sn_y/In_xAl_{1-x}As$(or Ge)/(100)2°GaAs heterostructures analyzed in this work: (A) 270 nm thick epitaxial Ge layer grown on 170 nm AlAs buffer on (100)/2° semi-insulating (S.I.) GaAs substrate; (B) 350 nm thick compressively strained $Ge_{0.97}Sn_{0.03}$ layer on 250 nm AlAs buffer; (C) 50 nm thick compressively strained $Ge_{0.94}Sn_{0.06}$ layer on 38 nm Ge; (D) 350 nm thick GeSn grown on 500 nm thick lattice-matched $In_{0.12}Al_{0.88}As/In_xAl_{1-x}As$/GaAs buffer layer.

power that impinged on the sample surface, considering the losses during transmission, was ~7 mW with a 100× objective lens and a diffraction grating size of 1800 g/mm (grooves per millimeter) used for detection of the scattered light. The instrument was calibrated using a standard Silicon sample, that exhibited a LO phonon mode peak at $\omega_{0,Si}$ = 520.67 cm^{-1},[44] with a spectral shift resolution of 0.003 cm^{-1}. The Raman data, representing inelastic Stokes scattering, was recorded by averaging over three iterations of 10 seconds each. For methodical analysis, the collected spectra of all the samples were normalized to a range of [0, 1] and mathematically fitted using the Lorentzian distribution function to precisely identify the peak position, avoiding artifacts associated with peak determination directly from the raw data. Using the lattice matched $Ge_{0.94}Sn_{0.06}/In_{0.12}Al_{0.88}As/GaAs(100)/2^{\circ}$ in *sample D*, strain-induced shifts due to phononic deformation potentials were analyzed to calculate the material parameter *b* linked to the biaxially strained crystal lattice overlayer of $Ge_{0.94}Sn_{0.06}$ in *sample C* with the same crystal orientation as the reference sample subject to the selection rules,[45] and same mole fractions of the elements. The phononic oscillation Raman peaks in *samples A* and *B* were also recorded to specifically study the effects of Sn atomic species on the crystal lattice vibrations in Ge and GeSn epilayers, as a broader perspective over a GeSn based optoelectronic device level application.

Optical properties of 6% Sn compositional $Ge_{0.94}Sn_{0.06}$ in *samples C* and *D*, 0.81% compressively strained and lattice matched, respectively, were studied using PL spectroscopy at 79 K temperature and 700 mW excitation power (corresponding to 7 nJ per pulse). The excitation source was a Ti:Sapphire laser operating at 720 nm with a repetition rate of 80 MHz and pulse duration of 140 fs, to generate photoexcited carriers. The laser spot size was ~250 μm in diameter. The PL emissions from these samples were collected by a Horiba spectrometer, connected to a liquid nitrogen-cooled InGaAs detector, using a standard Lock-in technique with a modulation frequency of 335 Hz using a mechanical chopper. Deconvolution of the multiple Gaussian peaks was performed using Origin Pro 2022b. The analysis showed shifts in the radiative (direct, Γ) and non-radiative (indirect, *L*) transition energies due to 6% Sn in GeSn compared to epitaxial Ge layer of *sample A*.[46] Also, the compressive strain induced blue shifts in the $Ge_{0.94}Sn_{0.06}$ emission peaks from Γ–valley were observed, which asserted the need of a lattice matched GeSn/InAlAs material system.

Later, the chemical effects of Sn were studied through bonding properties of the topmost epitaxial layers in *samples A–D* were investigated using a PHI Quantera SXM-03 (Scanning XPS Microprobe) system powered by a monochromatic Al–Kα (1486.7 eV) X-ray source. A low energy (0 to 10 eV) electron gun neutralized the positive charges accumulated (due to the loss of electrons during photoemission) in the samples throughout the XPS spectral acquisition. In a system without the charge neutralization feature, a continuous charge induced shift will be observed in the binding energies of the CLs spectra during data collection. The consistency in Ge 3d CL peak position during the long spectral acquisition period of ~30 minutes prove that the accumulated positive charges were compensated by the low energy electron gun. The photoemission spectra were collected with a pass energy of 26 eV by a hemispherical electron energy analyzer at an exit angle of 45° with respect to the normal to sample surface. Prior to loading the samples into the XPS chamber, each of them was wet-chemical-etch cleaned by deionized water for 10 secs to clean the sample surface. The acquired XPS spectral peaks were fitted using CasaXPS 2.3.25 tool by convolution of Lorentzian and Gaussian functions – where ideally a pure Lorentzian line shape represents a metal and a pure Gaussian line shape, a compound.[47] The inelastically scattered regions (*i.e.*, photoemission peaks from inelastically emitted electrons) were fitted with an Iterated Shirley background. The elemental CL binding EDCs and valence band maxima (VBM) were carbon corrected with the adventitious C 1s CL at its standard peak position of 285 eV.[48]

Chemical shifts towards the lower binding energy side were observed for Ge 3d CL states from all the epitaxial GeSn *samples B–D* (their peak positions are assigned with respect to the VBM of respective samples). This was attributed to different strength of Ge–Ge and Ge–Sn bonds in GeSn alloy than the only Ge–Ge bonds in an elemental Ge material. Note that the tendency of a Sn atom bonding with another Sn atom is very less at such a low composition (3%, 6%),[49] hence a Sn–Sn chemical bond is not considered here. Lower electronegativity of Sn atomic species with the same valency as Ge atoms, tends to shift the BE of the Ge 3d CLs to the lower energy side.[50] After studying the chemical bonding properties of Ge in the top epitaxial GeSn layer, the lattice matched $Ge_{0.94}Sn_{0.06}/In_{0.12}Al_{0.88}As$ heterostructure material system (*sample D*) was probed to determine the bonding of Ge at the heterointerface. The 350 nm thick layer of $Ge_{0.94}Sn_{0.06}$ was sputter etched using Ar^{+} ion gun at a low voltage of 1 kV over a 2 mm × 2 mm raster sized area to reach deep and far into the epitaxial layer discovering the $Ge_{0.94}Sn_{0.06}/In_{0.12}Al_{0.88}As$ heterointerface. Once the XPS spectra was acquired from the interface, more sputtering was done till the spectra revealed only the elemental peaks native to the constant composition $In_{0.12}Al_{0.88}As$ buffer, specifically to probe

the BEs of As 3d CL. To evaluate the ΔE_V, the binding energy peak positions of the CL states from three regions of the material were needed, namely: (a) Ge 3d, Sn 4d {top $Ge_{0.94}Sn_{0.06}$ epilayer}; (b) Ge 3d, Sn 4d, As 3d {heterovalent $Ge_{0.94}Sn_{0.06}/In_{0.12}Al_{0.88}As$ interface}; and (c) As 3d {bottom $In_{0.12}Al_{0.88}As$ layer}, along with the VBMs of each region. ΔE_V was calculated using Kraut's method,[51] and ΔE_C deduced from this measured ΔE_V and the bandgaps of $Ge_{0.94}Sn_{0.06}$[52] and $In_{0.12}Al_{0.88}As$[53] semiconductors. By this method, the lattice matched $Ge_{0.94}Sn_{0.06}/In_{0.12}Al_{0.88}As$ heterostructure material system was dissected to experimentally study the conducive nature of electro-optical carrier confinement, required for group IV GeSn based optoelectronic applications.

Results and Discussion

(A) Raman spectral analysis in $Ge_{1-y}Sn_y$

Characterizing the semiconducting crystals for inelastic scattering phenomena using Raman spectroscopy has gained attention over decades to analyze the structural and the vibrational properties.[54, 55] Strain state in a crystal lattice is determined using non-destructive Raman measurements as an immediate application in electronic and photonics.[55] The frequency of quanta of vibrations, *i.e.,* phononic frequencies, are observable only for the long wavelength (k=0) Ge–Ge LO phonon modes in (100) oriented cubic semiconductor crystals.[56] A cubic semiconductor crystal like Ge has threefold degenerate optical phonon modes in a strain free state. This degeneracy is split into a doublet and a singlet mode under the influence of the biaxial strain due to the tetragonal deformation potential.[45] Here, Raman spectroscopy measurements were performed in the backscattering geometry to understand the physical effects of Sn atoms on the crystal lattice vibrations in GeSn alloy. The accompanying Raman Stokes scattering frequency of Ge–Ge LO phonon mode in a control bulk sample of *n-type* Ge with doping concentration of 6×10^{16} cm^{-3} was determined to be $\omega_0 = 300.2 \pm 0.01$ cm^{-1}, standard Raman wavenumber for Ge crystal lattice,[39] as shown in **Fig. 2**. Similarly, for the epitaxial Ge layer in *sample A* it was obtained at $\omega_{0,sample\ A} = 300.02 \pm 0.01$ cm^{-1}. Apart from the effect of compressive strain, there is an additional effect of Sn atoms on the positions of Ge–Ge LO phonon modes: $\omega_{0,sample\ B} = 298.66 \pm 0.03$ cm^{-1} and $\omega_{0,sample\ C} = 299.6 \pm 0.03$ cm^{-1}. As inferred from the wavenumber shifts ($\Delta\omega$) compared to the no strain phonon frequency in *sample A* and bulk Ge, the vibrational properties of these samples are more influenced by the Sn composition than strain, vividly supported by the literature[57] and compliance tensor elements related to the compressive strain shifting the peaks to the higher wavenumber side.[58] Also, it is an additional tool to categorically identify the lattice arrangements in *samples B* and *C* as different to a Ge lattice in *sample A* or the control bulk Ge sample.

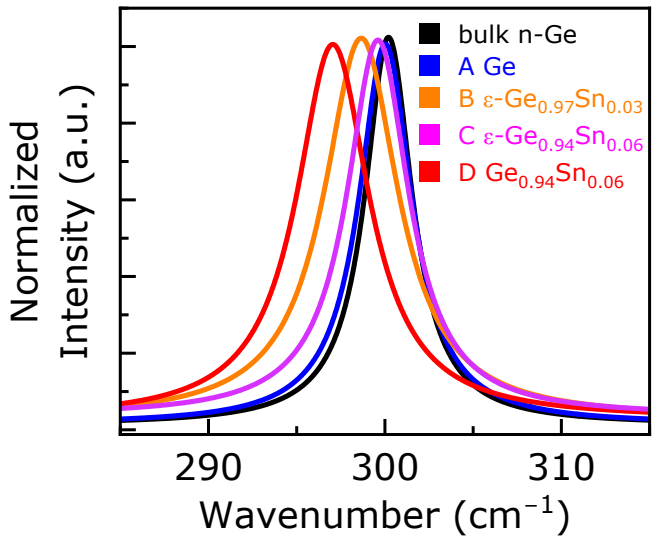

Fig. 2: Raman spectra recorded in the (100) backscattering geometry to study the vibrational properties of the $Ge_{1-y}Sn_y$ *samples A–D,* plot shows Ge–Ge LO phonon mode wavenumbers. Using strain free $Ge_{0.94}Sn_{0.06}$ epilayer of *sample D* and 0.81% strain in $Ge_{0.94}Sn_{0.06}$ of *sample C*, the wavenumber shift of $\Delta\omega = 2.55$ cm^{-1} gives material parameter $b = 314.81$ cm^{-1} for 6% Sn compositional $Ge_{0.94}Sn_{0.06}$.

The Ge–Ge LO phonon mode peak in *sample C* ($Ge_{0.94}Sn_{0.06}$) $\omega_{0,sample\ C} = 298.66$ cm^{-1} has higher Raman shift than *sample B* ($Ge_{0.97}Sn_{0.03}$) $\omega_{0,sample\ B} = 299.6$ cm^{-1} with reference to the bulk Ge sample, $\omega_0 = 300.2 \pm 0.01$ cm^{-1}. There are multiple factors contributing to this difference in Raman shifts that could not be attributed to singular reason. The effect of alloy composition ($\Delta\omega_{Alloy}$) and strain ($\Delta\omega_{Strain}$) on the total Raman shift ($\Delta\omega$), with reference to their linear relations for a semiconductor crystal is represented by[58]:

$$\Delta\omega = \Delta\omega_{Alloy} + \Delta\omega_{Strain} = a \cdot x + b \cdot \varepsilon_{||} ;$$

where parameter a weighs the alloy composition (here x is Sn%) and parameter b weighs the in-plane strain ($\varepsilon_{||}$) contributions to the total Raman shift ($\Delta\omega$). It is essential to know established standard values of a and b with reference to either a bulk material or a virtually defect-free lattice matched semiconductor material to decouple their relative contributions.[59] Here, to determine the standard value of a, it is necessary to grow a range of lattice matched GeSn semiconductor systems with different Sn (x %) compositions that helps decoupling the contribution of alloy composition on Raman shift. Similarly, to determine a standard b value for the reference composition, it is prudent to synthesize a lattice matched and a strained GeSn semiconductor material system with same composition, that helps decoupling the contribution of strain to Raman shift. For instance, to find

b for *x* = 6% using $\varepsilon_{\parallel}$ = 0.81% in *sample C* ($Ge_{0.94}Sn_{0.06}$/Ge) it was essential to synthesize a lattice matched *sample D* ($Ge_{0.94}Sn_{0.06}/In_{0.12}Al_{0.88}As$), as explained hereafter.

Strain calculations using Raman spectroscopy is widely endorsed using the relation, $\Delta\omega = -b \cdot \varepsilon_{\parallel}$ cm^{-1}, where *b* (cm^{-1}) is a material parameter representing the phonon deformation potentials, compliance tensor elements and the strain-free phonon frequency (ω_0); and $\varepsilon_{\parallel}$ is the in-plane strain component. The material parameter *b*, for a relaxed GeSn is yet to arrive at a universal standard value within the scientific community.[59] In this work, *sample D* has a lattice matched epitaxial $Ge_{0.94}Sn_{0.06}$ layer and *sample C* has 0.81% compressively strained epitaxial $Ge_{0.94}Sn_{0.06}$ layer, both having same Sn composition of 6%. This allows one to do the reverse computation of the material parameter *b*, as the strain value $\varepsilon_{\parallel}$ is known from HR-XRD and the wavenumber shift $\Delta\omega$ taken with *sample D*'s unstrained phonon frequency ω_0 acting as the reference point. Using these values: $\omega_{0,sample\ D}$ = 297.05 ± 0.03 cm^{-1}, $\Delta\omega$ = 2.55 ± 0.06 cm^{-1}, and $\varepsilon_{\parallel}$ = 0.81 %, we calculate the material parameter *b* for a 6% Sn compositional GeSn as $b_{Ge0.94Sn0.06} \approx 314.81 \pm 14$ cm^{-1}. This compels one to prefer a lattice matched GeSn material for optoelectronic applications as there is more reduction in the phononic vibrations within a lattice matched epitaxial GeSn layer than a strained layer. Hence, one expects improved quantum efficiency in a photodetector and reduced threshold current density in a laser fabricated using GeSn active region similar to the lattice matched *sample D* ($Ge_{0.94}Sn_{0.06}/In_{0.12}Al_{0.88}As$) material system where loss due to the phononic interactions in the *L*–valley is reduced. This study was related to the physical effects of Sn atomic species on Ge in GeSn alloy and in the next section, the optical properties of the 6% Sn compositional *samples C* and *D*, studying the effects of Sn on the radiative and non-radiative transitions are presented.

(B) Optical properties of $Ge_{0.94}Sn_{0.06}$ by PL

Characterization of semiconductor materials using PL spectroscopy gives information on optical properties and quality of the material, and this technique is used as a prominent tool over decades.[53, 60, 61] Direct and indirect energy bandgap transitions, respectively, dominating the radiative and non-radiative recombination dynamics of the semiconductors, are explicitly characterized from the PL emission spectra.[62] Here, the PL measurements were performed at 79 K that allowed to observe the effect of Sn atomic species on the emission spectra originating from epitaxial $Ge_{0.94}Sn_{0.06}$ layers in *samples C* and *D*, having 6% Sn concentration, as shown in **Fig. 3 (a)** and **(b)**, respectively. The deconvoluted optical transition peaks in *sample C*, shown in **Fig. 3 (a)**, represent emission peaks from both the top 50 nm thick ~ 0.81 % compressively strained epitaxial $Ge_{0.94}Sn_{0.06}$ layer and the bottom 38 nm epitaxial Ge layer, grown on GaAs substrate. The peaks identified at 0.762 eV and 0.683 eV are from respective Γ-*lh/hh* and *L*-*lh/hh* transitions in the Ge layer. This is confirmed by the PL spectral peak

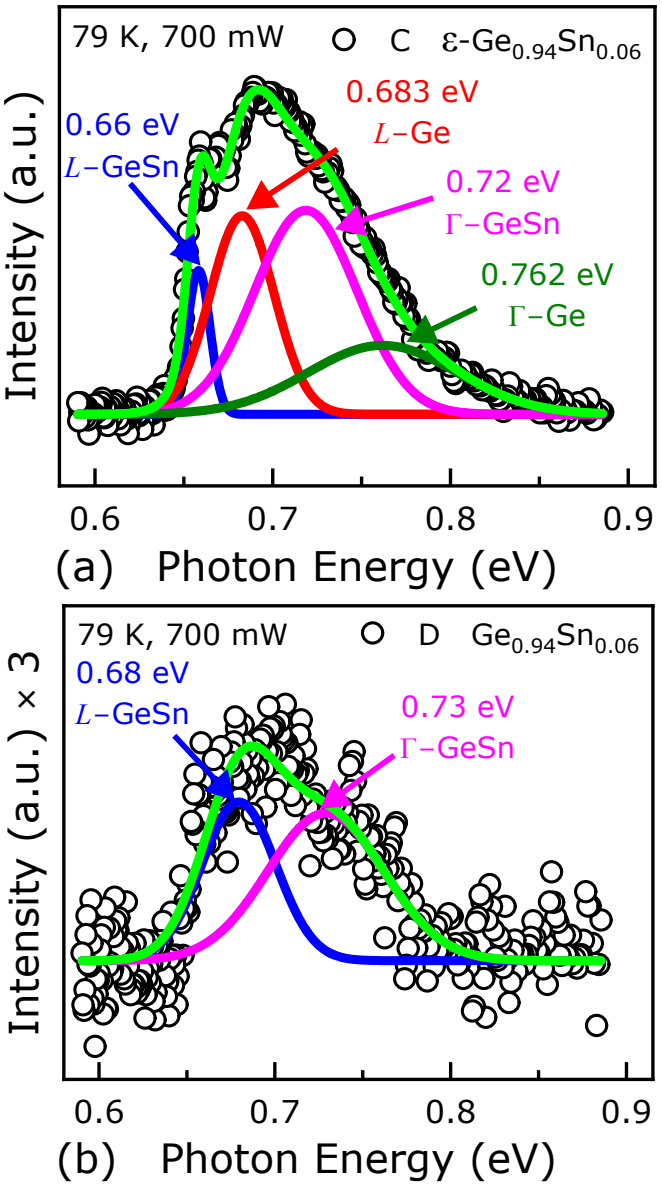

Fig. 3: Low temperature PL spectra at 79 K and 700 mW power from: (a) ~0.81% compressively strained 50 nm epitaxial $Ge_{0.94}Sn_{0.06}$ layer on 38 nm Ge of *sample C*. *L-hh* and Γ-*hh* transition peaks from 50 nm $Ge_{0.94}Sn_{0.06}$ having strain induced split of *hh* above *lh*, and *L-lh/hh* and Γ-*lh/hh* peaks from 38 nm Ge are observed, (b) 350 nm thick lattice matched $Ge_{0.94}Sn_{0.06}$ epilayer of *sample D*. Only *L-lh/hh* and Γ-*lh/hh* transition peaks are observed with *lh-hh* degeneracy maintained in 350 nm thick layer, with no peaks from the underlying large bandgap (indirect, X) $In_{0.12}Al_{0.88}As$ constant composition buffer layer.

positions in epitaxial Ge of *sample A* at 77 K,[46] where the Γ–valley was 0.11 eV above the *L*–valley. Whereas the other two peaks, located at 0.72 eV and 0.66 eV, are attributed to the photoemission peaks from the Γ-*hh* and *L*-*hh* transitions in the *lh*-*hh* degeneracy split (*hh* above *lh*) ~0.81% compressively strained epitaxial GeSn layer. It is observed in the literature that compressive strain in GeSn lowers the *L*–valley and shifts the Γ–valley upwards,[63] thereby decreasing the indirect bandgap and increasing the direct bandgap energies in compressively strained $Ge_{0.94}Sn_{0.06}$, proved by the transitions noted from the PL experiments in the present work. Moreover, the respective peak assignments are explicitly confirmed by the Γ-*lh/hh* and *L*-*lh/hh* transitions at 0.73 eV and 0.68 eV, respectively, from the lattice matched *sample D* as shown in **Fig. 3 (b)**. Note that that Γ–*L* difference is 0.05 eV in lattice matched $Ge_{0.94}Sn_{0.06}$ and 0.06 eV in the ~ 0.81% compressively strained $Ge_{0.94}Sn_{0.06}$ layer, further supporting the compressive strain related Γ and *L* valley shifts. In addition, alloying 6% Sn to Ge brings it to the verge of converting into a direct band gap lattice matched $Ge_{0.94}Sn_{0.06}$ material, within 50 meV to such a transition at 79 K. It is imperative to acknowledge that at room temperature, Ge (with 0% Sn) has Γ–*L* difference of 136 meV[13] that is reduced to 50 meV at 79 K by adding 6% Sn to Ge, forming $Ge_{0.94}Sn_{0.06}$ alloy, further supporting that little higher Sn atomic concentration than 6% in the lattice matched GeSn[1–12] would aid the indirect to direct bandgap transition of Ge. In addition to increasing Sn concentration in GeSn alloy to achieve direct bandgap nature, it is necessary to confine the carriers electrically and optically within the active GeSn region to realize efficient group IV optoelectronic devices. In the succeeding sections, the chemical effects of Sn atomic species on the binding energies of the Ge core levels, and consequently, superior energy band alignment is presented.

(C) XPS analysis of $Ge_{1-y}Sn_y$

Shifts in the binding energy of the elemental core level states within a compound material arise due to the varying chemical potential from the bonding.[64] Such chemical shifts are observed clearly via XPS, and recorded in standard databases like NIST, PHI electronic handbook of photoemission spectral peaks.[64] The bonding environment of Ge in a GeSn alloy drifts away from the conventional all Ge–Ge bonds in an epitaxial or a bulk Ge. This deems it necessary to understand the following – heterointerfacial property, chemical stoichiometry, atomic interdiffusion, and nature of energy band alignment – in a $Ge_{1-y}Sn_y$/III-V material system. The bonding environment of group IV atomic species (Ge, Sn) to group III-V atomic species plays a crucial role in the heterointerfacial electronic structure, that can potentially drift away from the abrupt (stoichiometric) GeSn/III-V heterovalent interface.[34] This behavior was studied beginning with the collection of the XPS spectra originating from three epitaxial GeSn layers, namely: (i) a 350 nm thick compressively strained $Ge_{0.97}Sn_{0.03}$ layer grown on 250 nm AlAs buffer – *sample B*; (ii) a 50 nm thick compressively strained $Ge_{0.94}Sn_{0.06}$ layer grown on a 38 nm Ge layer – *sample C*; and (iii) a 350 nm thick lattice matched $Ge_{0.94}Sn_{0.06}$ layer grown on a 500 nm $In_{0.12}Al_{0.88}As$ buffer layer – *sample D*. From this acquired photoemission spectra, the binding energy peak positions of the spin-orbit split Ge ($3d_{3/2}$ and $3d_{5/2}$) and Sn ($4d_{3/2}$ and $4d_{5/2}$) CL states were determined by Lorentzian peak convolution fitting. The position of the VBM was obtained by linearly fitting the onset of photoemission spectra from the valence band density of states, which exhibits a response equivalent to a leading edge from a constant random background noise.[51]

The binding energy peak position of Ge $3d_{5/2}$ CL state from the reference *sample A* is 29.23 ± 0.05 eV.[43] Whereas similar peak positions for a 0.53% compressively strained $Ge_{0.97}Sn_{0.03}$/AlAs layer of *sample B*, 0.81% compressively strained $Ge_{0.94}Sn_{0.06}$/Ge layer of *sample C* and lattice matched $Ge_{0.94}Sn_{0.06}/In_{0.12}Al_{0.88}As$ of s*ample D* were identified to be 29.02 ± 0.05 eV, 29.13 ± 0.05 eV and 29.17 ± 0.05 eV, respectively, as shown in **Figs. 4(a-c)**. The chemical shift towards the lower binding energy is effectively attributed to the Ge atoms bonding covalently with Sn (same valency as Ge) which is less electronegative {χ_r(Sn) = 1.96}than Ge {χ_r(Ge) = 2.01}.[65] Here, the covalent nature of the Ge–Ge and Ge–Sn bonds remains intact with no change in a priori valency of both the elements, before and after their bonding to nucleate as GeSn. Similarly, chemical shifts were observed in the binding energy peak positions of Sn $4d_{5/2}$ CL states in *samples B*: 24.05 ± 0.05 eV, *C*: 23.89 ± 0.05 eV and *D*: 24.08 ± 0.05 eV, as logged in Table I. At a detection limit of 0.1–1% atomic composition, XPS shows relatively less intense energy distribution curves for 3% Sn (*sample B*) as to 6% Sn (*samples C, D*) that is clearly visible in **Fig. 4**. As the compressive strain in *samples B* and *C* is low, it was not possible to decouple the interpretation for alloying Sn to Ge and the biaxial strain that the epitaxial layers are subject to, from the XPS spectra. However, the lowering of the conduction band minima, that is concurrent with the Fermi level shifts, can be observed from the binding energy positions of the valence band maxima of Ge (*sample A*), $Ge_{0.97}Sn_{0.03}$ (*sample B*), and $Ge_{0.94}Sn_{0.06}$ (*sample C*) epitaxial layers as presented in Table I. Photoemission from valence band density of states were determined with reference to the Fermi level of the samples under

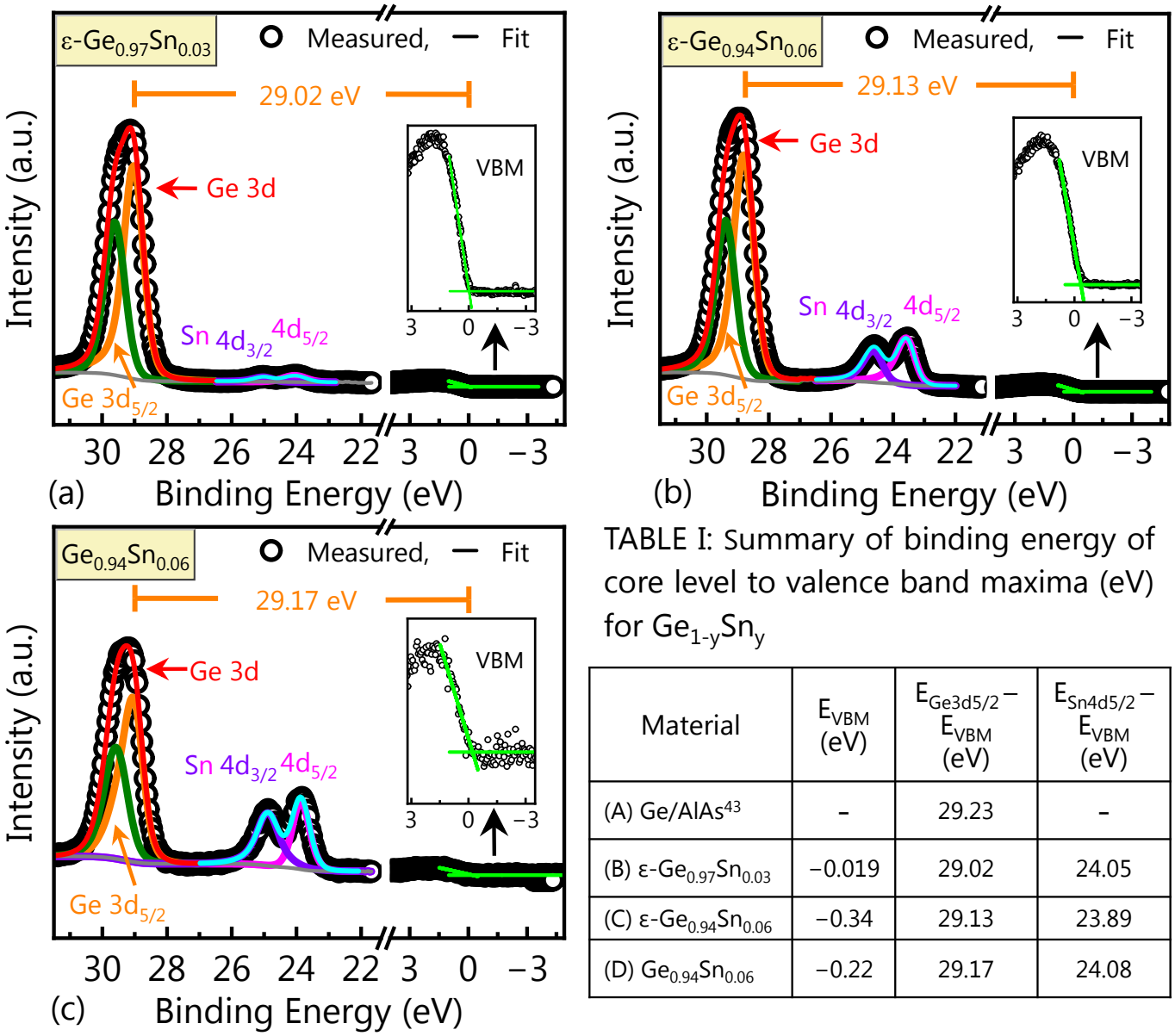

TABLE I: Summary of binding energy of core level to valence band maxima (eV) for $Ge_{1-y}Sn_y$

Material	E_{VBM} (eV)	$E_{Ge3d5/2} - E_{VBM}$ (eV)	$E_{Sn4d5/2} - E_{VBM}$ (eV)
(A) Ge/AlAs[43]	-	29.23	-
(B) ε-$Ge_{0.97}Sn_{0.03}$	−0.019	29.02	24.05
(C) ε-$Ge_{0.94}Sn_{0.06}$	−0.34	29.13	23.89
(D) $Ge_{0.94}Sn_{0.06}$	−0.22	29.17	24.08

Fig. 4: X-ray photoelectron spectroscopy (XPS) spectra of Ge 3d, Sn 4d CLs and valence band maximum from: (a) 350 nm thick compressively strained $Ge_{0.97}Sn_{0.03}$ layer on 250 nm AlAs buffer – *sample B*, (b) 50 nm thick compressively strained $Ge_{0.94}Sn_{0.06}$ layer on 38 nm Ge – *sample C*, (c) 350 nm thick lattice matched $Ge_{0.94}Sn_{0.06}$ layer on 500 nm $In_{0.12}Al_{0.88}As$ buffer layer – *sample D*.

examination.[51] $VBM_{sample\ C} = -0.22 \pm 0.05$ eV and $VBM_{sample\ D} = -0.34 \pm 0.05$ eV depict an earlier onset of the photoemission spectra from a compressively strained crystal lattice having heavy holes split above the light holes, where the decoupling stays obscure. After the preceding analysis, the succeeding sections specifically detail the XPS study of heterointerfacial region in the lattice matched $Ge_{0.94}Sn_{0.06}/In_{0.12}Al_{0.88}As$ material system of *sample D* and its constant composition $In_{0.12}Al_{0.88}As$ buffer layer. Wherein, the nature of energy band alignment profoundly impacted by the group IV and III-V interfacial stoichiometry is stated (*hereafter*, investigation of only the lattice matched $Ge_{0.94}Sn_{0.06}/In_{0.12}Al_{0.88}As$ heterostructure of *sample D* is presented).

(D) Sputter depth-dependent XPS analysis of lattice matched $Ge_{0.94}Sn_{0.06}/In_{0.12}Al_{0.88}As$

Low energy sputter depth profiling helps to reach the deep regions beyond the mean escape depth of the elements present in a layered semiconductor heterostructure. It made the interfacial region of the lattice matched $Ge_{0.94}Sn_{0.06}/In_{0.12}Al_{0.88}As$ structure in *sample D* accessible for evaluation of the interfacial stoichiometry and enter into the constant composition $In_{0.12}Al_{0.88}As$ buffer region. The top 350 nm thick $Ge_{0.94}Sn_{0.06}$ epitaxial layer was sputter etched to reach the $Ge_{0.94}Sn_{0.06}/In_{0.12}Al_{0.88}As$ heterointerface, as shown in **Fig. 5,** while simultaneously acquiring XPS spectra spanning the binding energy range 22 eV to 50 eV that

covers Ge 3d, Sn 4d and As 3d CL states**.** The sputter depth profiling, with duration, helped to calculate the time taken to sputter etch the 350 nm thick $Ge_{0.94}Sn_{0.06}$ epitaxial layer and reach the $Ge_{0.94}Sn_{0.06}/In_{0.12}Al_{0.88}As$ interface. After ~100 minutes, the sputtering rate of 6% Sn compositional $Ge_{0.94}Sn_{0.06}$ alloy was evaluated to be ~3.5 nm/min while using Ar^+ ion at 1 kV over an area of 2 mm × 2 mm raster (trajectory of sputtering) size. Unlike the scenario of photoemission without any sputtering, the residual surface (positive) charge gets accumulated faster than it can be compensated by the low energy electron gun. To overcome this, a charge shift correction was done with reference to the very first unsputtered spectral acquisition. In the foremost XPS spectra (*see* green color at ~23 min in **Fig. 5**), Ge energy loss lines are observed around ~ 45.7 eV as the photoelectrons lose energy during the interaction with other electrons on their way out of the sample surface.[64] However, as this region is located near the binding energy position of the main As 3d photoelectron lines, these Ge energy loss lines get submerged under the highly intense As 3d spectra as we approach the interface region. Low peak intensity for Sn 4d CL states (a deeper core level) were observed due to low atomic composition and it decayed faster to almost blend with the photoelectron background noise.

The intermediary XPS spectral acquisition was done to monitor the peak intensity from Ge 3d and Sn 4d CLs of the $Ge_{0.94}Sn_{0.06}$ epitaxial layer decaying and As 3d CL peak from the $In_{0.12}Al_{0.88}As$ emerging. The simultaneous presence of these three photoemission peaks demarcates the interfacial region. The reason for not selecting the other elements, indium or aluminum, is due to the MBE epitaxy growth conditions, where: an As_2 overpressure was preferentially maintained post–growth of InAlAs buffer layer, leading to an As-terminated III-V surface before shifting the wafer to group IV chamber (that is isolated from III-V chamber at ultra-high vacuum).[39] In addition, the bond formation energy of As–Ge is less than In–Ge or Al–Ge bonds.[34] Note that the peak intensities are represented in the normalized form, as the pass energy used for continuous spectral acquisition was higher (280 eV: low energy resolution) till ~95 min with preference given to identify the photoelectron lines of As 3d CL emerging from the underlying $In_{0.12}Al_{0.88}As$ buffer layer. With its emergence, the pass energy was lowered to 26 eV for higher energy resolution and the sputtering period was reduced, since a carefully measured approach was essential to collect the spectral information from heterointerface. This is evident from the full width at half maximum of Ge 3d photoelectron peaks being wider at

Fig. 5: XPS sputter depth profile of a 350 nm thick lattice matched $Ge_{0.94}Sn_{0.06}$ epitaxial layer grown on 500 nm $In_{0.12}Al_{0.88}As$ buffer layer, (*sample D*). Using Ar^+ ion gun at 1 kV over an area of 2 mm × 2 mm raster size, the sputtering rate of the GeSn alloy was determined to be ~3.5 nm/min. Acquisition of XPS spectra through the binding energy range, comprising core levels of Ge 3d, Sn 4d and As 3d states, shows the outreach to heterovalent heterointerface of lattice matched $Ge_{0.94}Sn_{0.06}/In_{0.12}Al_{0.88}As$ material system.

high pass energy (prior to ~95 min). When As 3d CL peak intensity was visibly same as that of Ge 3d CL, the heterointerfacial region is considered to be arrived at by sputtering. As soon as the interfacial region was reached, to precisely identify the band alignment type of $Ge_{0.94}Sn_{0.06}/In_{0.12}Al_{0.88}As$ heterostructure, further acquisition was done in multiple iterations (8 sweeps for each elemental CL and material VBM) at a high resolution pass energy of 26 eV. The method of constructing the energy band alignment at a heterovalent junction is presented in the next section.

(E) GeSn/InAlAs heterointerface band alignment

There exists a disparity in the construction of energy band alignment at heterojunctions between the theoretical and experimental methods, which leads to more reliability on the experimental techniques of optical absorption, x-ray photoelectron spectroscopy, ultraviolet photoelectron spectroscopy, and C-V characteristics.[66] XPS is used for precise band offset determination in compound semiconductor heterostructures, with each layer and the correlated interfaces of interest taken into consideration.[34] Subsequent to the XPS analysis of epitaxial GeSn layers, as stated in the previous section, it was imperative to analyze the nature of energy band alignment at the lattice matched $Ge_{0.94}Sn_{0.06}/In_{0.12}Al_{0.88}As$ heterointerface to quantitatively highlight the level of carrier confinement in the active region of GeSn. To this end, x-ray photoemission spectra required from three regions of the sample were acquired, namely: **(i)** the 350 nm $Ge_{0.94}Sn_{0.06}$ epitaxial layer; **(ii)** the $Ge_{0.94}Sn_{0.06}/In_{0.12}Al_{0.88}As$ heterovalent interface; and **(iii)** the 500 nm $In_{0.12}Al_{0.88}As$ constant composition buffer layer. Access to the latter two regions (heterointerface and constant composition InAlAs buffer) was made possible via low energy (at 1 kV) Ar^+ ion gun sputtering as discussed in the previous section. The XPS spectra acquired from $Ge_{0.94}Sn_{0.06}/In_{0.12}Al_{0.88}As$ interface [region (ii)] and $In_{0.12}Al_{0.88}As$ buffer [region (iii)] are represented in the **Figs. 6(a)** and **(b)**. Spectra of the top epitaxial $Ge_{0.94}Sn_{0.06}$ layer [region (i)] was analyzed earlier in section (B) [*see* **Fig. 4(c)**]. All the regions were mathematically quantified by the convolution of Lorentzian and Gaussian line shapes, revealing the binding energy peak positions of spin-orbit split Ge 3d $\{(E_{Ge\,3d\,5/2})^{Ge_{0.94}Sn_{0.06}}, (E_{Ge\,3d\,3/2})^{Ge_{0.94}Sn_{0.06}}\}$; Sn 4d $\{(E_{Sn\,4d\,5/2})^{Ge_{0.94}Sn_{0.06}}, (E_{Sn\,4d\,3/2})^{Ge_{0.94}Sn_{0.06}}\}$ and; As 3d $\{(E_{As\,3d\,5/2})^{In_{0.12}Al_{0.88}As}, (E_{As\,3d\,3/2})^{In_{0.12}Al_{0.88}As}\}$ CL states.

Likewise, the VBM spectra from each region, $(E_{VBM})^{Ge_{0.94}Sn_{0.06}}$ and $(E_{VBM})^{In_{0.12}Al_{0.88}As}$ was quantified by linearly fitting the photoemission take-off in the neighborhood of 0 eV binding energy. Using these quantified experimental values, the valence band offset (ΔE_V) was evaluated by the procedural method of Kraut *et al.*[51] as:

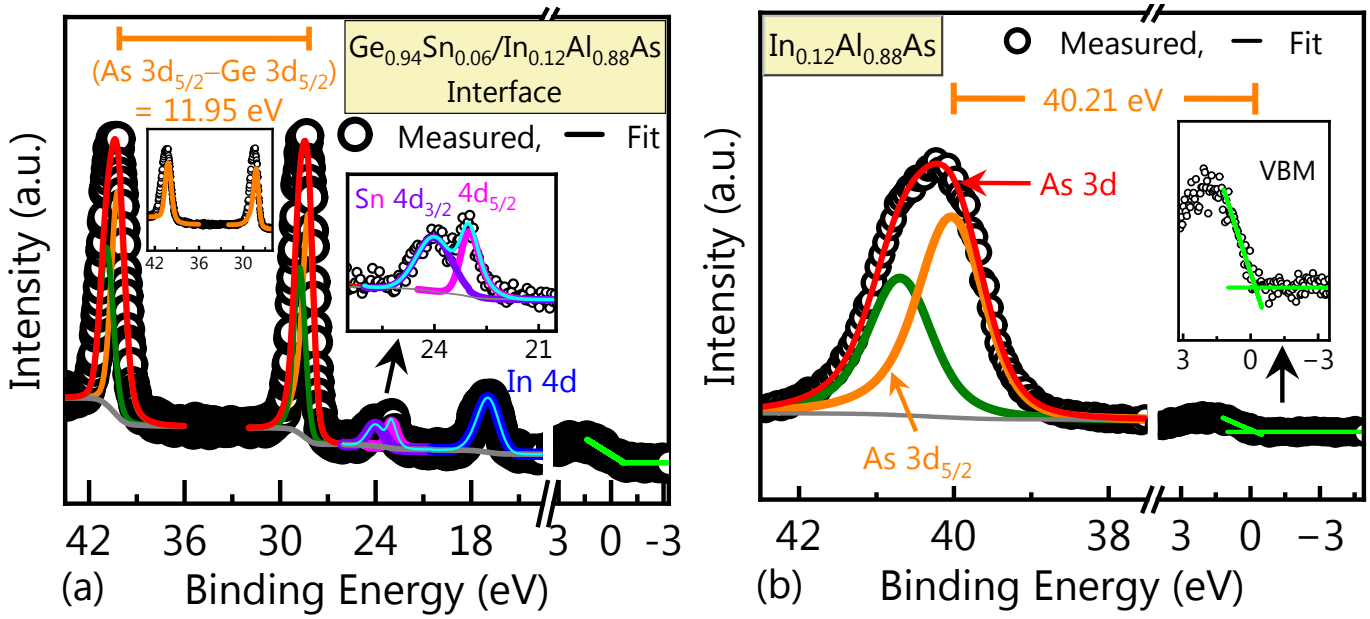

Fig. 6: X-ray photoelectron spectroscopy (XPS) spectra of: (a) Ge 3d, Sn 4d, As 3d and In 4d CLs and valence band maxima (VBM) depicting the binding energy separation between As $3d_{5/2}$ and Ge $3d_{5/2}$ CLs $(E_{As\,3d\,5/2} - E_{Ge\,3d\,5/2})^{interface}$ at the $Ge_{0.94}Sn_{0.06}/In_{0.12}Al_{0.88}As$ heterointerface; (b) As 3d CL and VBM $(E_{As\,3d\,5/2} - E_{VBM})^{In_{0.12}Al_{0.88}As}$ from the 500 nm $In_{0.12}Al_{0.88}As$ buffer layer of *sample D*.

$$\Delta E_V = (E_{Ge\,3d\,5/2} - E_{VBM})^{Ge_{0.94}Sn_{0.06}} - (E_{As\,3d\,5/2} - E_{VBM})^{In_{0.12}Al}$$

where,

$(E_{Ge\ 3d\ 5/2} - E_{VBM})^{Ge_{0.94}Sn_{0.06}}$ is the binding energy separation between Ge $3d_{5/2}$ CL and VBM of $Ge_{0.94}Sn_{0.06}$ epilayer, $(E_{As\ 3d\ 5/2} - E_{VBM})^{In_{0.12}Al_{0.88}As}$ of As $3d_{5/2}$ CL and VBM of $In_{0.12}Al_{0.88}As$ buffer layer, and $(E_{As\ 3d\ 5/2} - E_{Ge\ 3d\ 5/2})^{interface}$, notably, denotes the binding energy separation between the $3d_{5/2}$ CL states of Ge and As at the $Ge_{0.94}Sn_{0.06}/In_{0.12}Al_{0.88}As$ heterointerface. Each of these values in the same order are 29.17 ± 0.05 eV, 11.95 ± 0.05 eV and 40.21 ± 0.05 eV, respectively, as shown in **Fig. 7**. The valence band offset was calculated to be ΔE_V = 0.91 ± 0.1 eV for an unstrained/lattice matched GeSn epilayer having degenerate light hole – heavy hole valence bands.[9] So, this lattice matched $Ge_{0.94}Sn_{0.06}/In_{0.12}Al_{0.88}As$ heterostructure material system offers large barrier to confine the holes, thereby reducing their leakage to the underlying InAlAs buffer layer. As far as the electrons were concerned, $\Delta E_{C,\Gamma-X}$ at the GeSn Γ–valley to InAlAs X–valley was deduced from the bandgaps of GeSn, $E_{g,\Gamma}^{Ge_{0.94}Sn_{0.06}} = 0.6\ eV$[52] and InAlAs, $E_{g,X}^{In_{0.12}Al_{0.88}As} = 2.15\ eV$[53] using:

$$\Delta E_{C,\ \Gamma-X} = E_{g,X}^{InAlAs} - E_{g,\Gamma}^{GeSn} - \Delta E_V.$$

This value is evaluated to be $\Delta E_{C,\ \Gamma-X}$ = 0.64 ± 0.1 eV, $E_{g,X}^{In_{0.12}Al_{0.88}As} = 2.15\ eV$, the ΔE_C is $\Delta E_{C,\ L-X}$ = 0.66 ± 0.1 eV. In both the cases, a type–I straddling band alignment is achieved. Hence, this lattice matched $Ge_{0.94}Sn_{0.06}/In_{0.12}Al_{0.88}As$ heterostructure material system is suitable for optoelectronic applications targeting superior confinement of both types of carriers, electrons and holes. As a whole, this system is a viable candidate to realize a photodetector and a laser, both having a virtually defect–free interface lowering the leakage of carriers from the active region to the layer underneath. The large band offsets at both the conduction and valence bands makes it (the $Ge_{0.94}Sn_{0.06}/In_{0.12}Al_{0.88}As$ material system) better equipped to withstand potential changes in band alignment type caused by defects or atomic interdiffusion assisted deviations in the local bonding environment at the interface. Further expansion on the details of local bonding environment and interfacial stoichiometry, with regards to the inter layer atomic diffusion, is provided in the next section by comparing the band offset values obtained here to the theoretically computed first-principles calculations,[34] that model As up-diffusion from 0 (abrupt interface) monolayer (ML0) up to 2 monolayers (ML2). Wherein, the calculations assimilated the variations in valence band offsets due to mixed interfacial monolayer diffusion of atomic elements

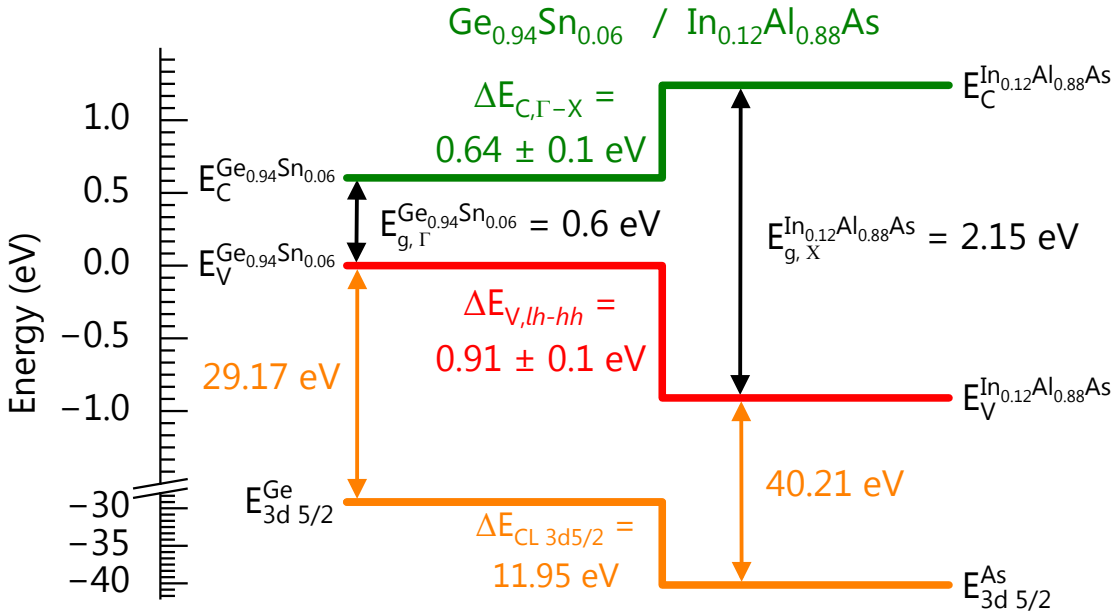

Fig. 7: Schematic energy band alignment of the lattice matched $Ge_{0.94}Sn_{0.06}/In_{0.12}Al_{0.88}As$ heterostructure at GeSn, representing large band offset values of ΔE_V = 0.91 ± 0.1 eV and $\Delta E_{C,\Gamma-X}$ = 0.64 ± 0.1 eV confining both the carriers within the active region of $Ge_{0.94}Sn_{0.06}$ epilayer.

that acts as a barrier to the leakage of photogenerated or injected electrons (in lasing). The schematic construction of the energy band lineups at the $Ge_{0.94}Sn_{0.06}/In_{0.12}Al_{0.88}As$ heterointerface, represented at the direct band Γ-valley, is shown in **Fig. 7.** Likewise, considering the minimum bandgap valley (the indirect *L*) for both GeSn $E_{g,L}^{Ge_{0.94}Sn_{0.06}} = 0.58\ eV$ and InAlAs from either side of the $Ge/In_xAl_{1-x}As$ heterointerface.

(F) Atomic interdiffusion at lattice matched $Ge_{1-y}Sn_y/In_xAl_{1-x}As$ heterointerface

Atomic interdiffusions at the semiconductor heterojunctions realign the energy bands with potentially measurable impacts observed on the band offset values

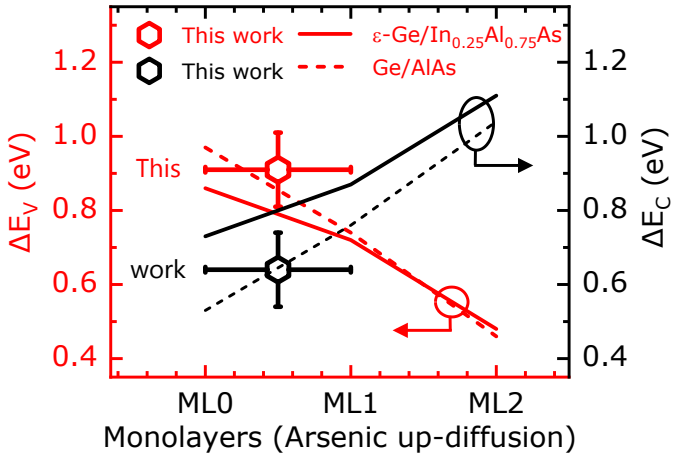

Fig. 8: Experimentally determined valence band offset (ΔE_V) and conduction band offset (ΔE_C) in the lattice matched $Ge_{0.94}Sn_{0.06}/In_{0.12}Al_{0.88}As$ heterostructure of the present work are presented (symbols with related error) as a function of monolayer Arsenic (As) up-diffusion into epitaxial GeSn layers. The decreasing and increasing line trends correspond to ΔE_V and ΔE_C, respectively, from first-principles-based calculations of atomic layer diffusion in Ge/AlAs and ε-$Ge/In_{0.25}Al_{0.75}As$.[34]

(ΔE_V, ΔE_C).[34] Such inter layer diffusions disrupt the chemical stoichiometry of the local bonding environment at the interface, that implicitly affects confinement of the carriers on either side of the bandgap depending on which atom diffused into which layer and number of monolayers. Theoretical (first-principles-based calculations) study[34] of 0-2 monolayer diffusions (ML0-ML2) of As into Ge at the $Ge/In_xAl_{1-x}As$ interface and experimental result in alignment has been reported.[39] With increasing As up-diffusion into Ge monolayers, the ΔE_V decreases and ΔE_C increases modifying the type of band alignment at higher diffusions during growth. Based on the caution exercised during the epitaxy growth conditions, maintaining the dimer As_2 overpressure prior to the III-V wafer transfer to the group IV chamber conforms to the preferred MBE growth process of III-V surface being As-terminated. This is further supported by the fact that As atoms bond with Ge at low formation energies than the other elements in its local environment.[39] Herein, interfacial stoichiometry of $As_{0.5}Ge_{0.5}$ was considered for the analysis of As up-diffusion into the epitaxial $Ge_{0.94}Sn_{0.06}$ layer.

The lattice matched $Ge_{0.94}Sn_{0.06}/In_{0.12}Al_{0.88}As$ heterostructure, in this work, is compared to the modeled mixed monolayer diffusion trend lying between Ge/AlAs and the ε-$Ge/In_{0.25}Al_{0.75}As$, as shown in **Fig. 8**. The band offset numerals measured here (ΔE_V = 0.91 eV, ΔE_C = 0.64 eV) are presented alongside the theoretical range of As up-diffusion from ML0 to ML2.[34] The interface abruptness and As up-diffusion into GeSn overlayer was deduced based on the low growth temperatures of GeSn epitaxial layers studied in this work (190 ˚C to 250 ˚C), and the linear response theory[34, 67, 68] incorporating the effect of Sn. In general, growth temperature during MBE is an essential parameter affecting the abruptness of an interface.[69] We had recently reported pristine heterointerfaces using atom probe tomography (APT) analysis of 1.6% ε-Ge on $In_{0.24}Ga_{0.76}As$[70] and B-doped Ge/AlAs/GaAs[43] heterostructures, where both epitaxial Ge layers were grown at 400 ˚C. Here, the growth temperature referred to was the thermocouple temperature. It was noted that there was no explicitly quantifiable evidence to show interdiffusion beyond ~ 6 Å diffusion window in both ε-Ge and B-doped Ge overlayers. In this work, the growth temperatures for epitaxial GeSn in samples *B*, *C* and *D* were 200 ˚C, 195/190 ˚C, and 250 ˚C, respectively. Therefore, we believe that the atomic interdiffusion in epitaxial $Ge_{1-x}Sn_x$ samples should be < 6 Å.

In order to predict the As up-diffusion into GeSn overlayer by incorporating the effect of Sn, the first-principles calculations of band offsets at an heterovalent interface computed using density functional theory (DFT) with Green Coulomb (GW) approximation[34] was used, where the ΔE_V at the GeSn/InAlAs heterointerface is represented as[67, 68]:

$$\Delta E_V = E_{V,\,GeSn} - E_{V,\,InAlAs} + \Delta(\delta E_V) + dV;$$

where $E_{V,\,GeSn}$ and $E_{V,\,InAlAs}$ are valence band maxima of the respective bulk layers, $\Delta(\delta E_V)$ is the GW approximation related self-energy correction factor, and the last term dV is the offset in the self-consistent potential across the interface. The term dV for As up-diffusion into GeSn layer, computed based on the linear response theory for interface diffusion, is given by[67, 68]:

$$dV(\text{As-GeSn}) = -\frac{\pi e^2}{2a_0\varepsilon}(0.5 + 2S);$$

where a_0 is the lattice constant of GeSn-InAlAs alloy and ε is its dielectric constant, S is the interfacial stoichiometry subject to charge neutrality at the interface, and e is the electronic charge. The lattice constant and dielectric constant of GeSn is greater than Ge, that makes dV(As-GeSn) less negative than dV(As-Ge). Although there is no first-principles calculations to show the offset term dV(As-GeSn) to be lower, this behavior is observed qualitatively from XPS measurement carried out in the present work. Elaborating on that, ΔE_V evaluated using 6% Sn 4d CL states, gives $\Delta E_V = 0.96 \pm 0.1$ eV whereas using 94% Ge 3d CL states it was evaluated as $\Delta E_V = 0.91 \pm 0.1$ eV. The 0.05 eV difference between these values corresponds to the dV(As-GeSn) term being less negative than dV(As-Ge) term, which supports the linear response theory applied to As up-diffusion into the GeSn overlayer with the effect of Sn taken into account. Similar results, experimental and first-principles based calculations, were demonstrated for B-doped Ge grown on AlAs.[43] When a Boron atom replaces a Ge atom, it results in a deficiency of 1/4th electron in each bond, whereas a lesser electronegative Sn atom replacing Ge atom results similar qualitative behavior, that is a Ge–Sn bond has weakly bound electrons affecting the band offsets at the interface. This effect was computed as a separate work by Pavarelli *et al.*,[71] where the dependence of band offsets on the electronegativity of the layer in contact with Ge at the heterointerface was performed using first-principles calculations.

With the explicit evidences reported above, the experimentally determined ΔE_V for $Ge_{0.94}Sn_{0.06}/In_{0.12}Al_{0.88}As$ was deduced to lie between ML0 and ML1, as shown in **Fig. 8**. From the first-principles calculations, the change in ΔE_V due to increase in As-up diffusion from ML0 (abrupt heterointerface) to ML1 (As up-diffusion limited to 1 monolayer) for Ge/AlAs was reported as 0.23 eV and for ε-$Ge/In_{0.25}Al_{0.75}As$ it was 0.14 eV.[34] In this work, the $In_{0.12}Al_{0.88}As$ layer has the substrate stoichiometry in between the stoichiometries of AlAs and $In_{0.25}Al_{0.75}As$ that follow the linear response theory applied to interface diffusion. The extent of As up-diffusion lying between ML0 (abrupt interface) and ML1 lends support to the growth physics that low MBE substrate temperature for GeSn vis-à-vis Ge reduced the inter layer diffusion of As atoms, by suppressing As up-diffusion, deterring the band–alignment modification.[31] Hence, lattice matched $Ge_{0.94}Sn_{0.06}/In_{0.12}Al_{0.88}As$ heterostructure offers threefold benefits: (i) a virtually defect-free active layer of GeSn; (ii) large band offsets (ΔE_V, ΔE_C); and (iii) highly immune to atomic interdiffusion stimulated shifts in band offsets and band alignment type.

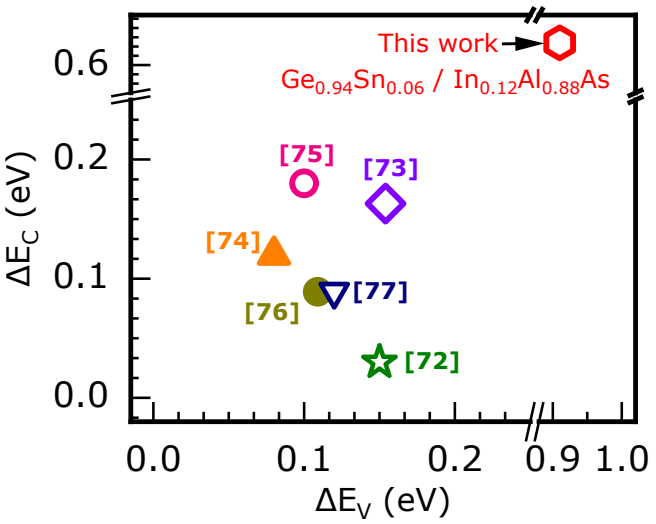

Ref.	Structure
[72]	$Ge_{0.92}Sn_{0.08}$ / Ge
[73]	$Ge_{0.85}Sn_{0.15}$ / Ge
[74]	$Ge_{0.92}Sn_{0.08}$ / Ge
[75]	$Ge_{0.84}Sn_{0.16}$ / $Si_{0.10}Ge_{0.75}Sn_{0.15}$
[76]	$Ge_{0.92}Sn_{0.08}$ / Ge
[77]	$Ge_{0.92}Sn_{0.08}$ / Ge

Fig. 9: Valence and conduction band offsets, ΔE_V and ΔE_C, at heterojunctions of GeSn grown on group IV small bandgap materials compared to $Ge_{0.94}Sn_{0.06}$ grown on large bandgap $In_{0.12}Al_{0.88}As$ material system analyzed in this work.

Highlighted in **Fig.9** are the band offsets of different GeSn material systems, with isovalent interfaces, grown on small bandgap materials like Ge and SiGeSn, next to the heterovalent interface $Ge_{0.94}Sn_{0.06}/In_{0.12}Al_{0.88}As$ material system studied in this work. It showcases that large barrier heights are attainable with the heterovalent systems: $\Delta E_V = 0.91$ eV and $\Delta E_{C,\Gamma-X} = 0.64$ eV, whereas the isovalent systems have both ΔE_V and $\Delta E_{C,\Gamma}$ less than 0.2 eV, affirming superior confinement to both types of carriers in the $Ge_{0.94}Sn_{0.06}/In_{0.12}Al_{0.88}As$ material system, preferred for efficient optical transitions. Hence, the possibility of realizing a group IV GeSn based quantum well laser that operates efficiently at room temperature becomes more real with a lattice matched $Ge_{1-y}Sn_y/In_xAl_{1-x}As$ material system that is tunable by varying Sn composition (and corresponding In composition to match the lattice constant).[31]

Conclusion

GeSn alloy is at the focal point of materials research for Si-compatible optoelectronics. It is essential to achieve superior carrier confinement in the conduction and valence bands of GeSn active region. In this work,

the role of Sn in carrier confinement of epitaxial GeSn material systems grown on (100)/2˚ GaAs substrates was analyzed. Physical effect of Sn atomic species was studied using Raman spectroscopy, that showed a red shifted wavenumber of Ge–Ge longitudinal optical phonon mode peak due to Sn with respect to a bulk Ge. Deformation potential, compliance tensor elements and strain free phonon frequency related to material parameter b for a $Ge_{0.94}Sn_{0.06}$ alloy was determined to be b = 314.81 ± 14 cm^{-1}, with the lattice matched $Ge_{0.94}Sn_{0.06}/In_{0.12}Al_{0.88}As$ heterostructure used as a reference. The effect of Sn and compressive strain on the optical properties of 6% Sn compositional GeSn heterostructure material systems, a ~ 0.81% compressively strained $Ge_{0.94}Sn_{0.06}$ layer and a lattice matched $Ge_{0.94}Sn_{0.06}$ epitaxial layer, were studied using PL spectroscopy at 79 K temperature and 700 mW laser power (corresponding to a laser fluence of 35 μJ/cm^2). Direct band Γ–valley transitions were observed at 0.72 eV and 0.73 eV in compressively strained and lattice matched epitaxial $Ge_{0.94}Sn_{0.06}$ layers, respectively. Whereas indirect band L–valley transitions were observed at 0.72 eV and 0.73 eV in compressively strained and lattice matched epitaxial $Ge_{0.94}Sn_{0.06}$ layers, respectively. Moreover, Sn induced red shifts and strain induced blue shifts in the photoemission spectral peaks were observed. Chemical effect of Sn atomic species was studied using X-ray photoelectron spectroscopy analysis, that showed the Ge core level binding energy distribution curves shifted to lower energy by Sn atoms. Such a shift affects the nature of local bonding environment at the $Ge_{0.94}Sn_{0.06}/In_{0.12}Al_{0.88}As$ heterointerface. In order to determine the energy band alignment of this heterostructure, sputtered depth profiling was carried out at ~3.5 nm/min using low energy Ar^+ ion gun (1 kV). The resulting band alignment was determined to be type–I with large band offsets of ΔE_V = 0.91 ± 0.1 eV and $\Delta E_{C,\Gamma-X}$ = 0.64 ± 0.1 eV. Analyzing these band offsets with first-principles-based calculations showed that $Ge_{0.94}Sn_{0.06}/In_{0.12}Al_{0.88}As$ material system has a pristine heterointerface with As up-diffusion limited to less than one GeSn monolayer, ruling out the possibility of atomic layer diffusion to a greater extent and defect assisted changes to band alignment. Furthermore, these band offsets were benchmarked with GeSn heterostructures grown on group IV materials, and it was found to be higher than the values reported in the literatures. Therefore, a lattice matched GeSn/InAlAs heterostructure material system with large band offsets, offers superior carrier confinement for efficient group IV optoelectronics.

Conflicts of interest

There are no conflicts to declare.

Acknowledgments

M. K. H. and S.K. acknowledge partial support from the NSF under grant number ECCS-2042079, a US-Ireland Joint R&D Program and Virginia Tech Nanofabrication facilities for assistance during materials analysis. G. A. K and Y. P. acknowledge support from the L. C. Hassinger Fellowship.

Notes and references

1 K. Wada and L. C. Kimerling (Editors), *Photonics and Electronics with Germanium*, Wiley-VCH, 2015.

2 S. Gupta, B. Magyari-Köpe, Y. Nishi, and K. C. Saraswat, *J. Appl. Phys. (Melville, NY, U.S.)*, 2013, **113**, 073707.

3 S. Xu, W. Wang, Y.-C. Huang, Y. Dong, S. Masudy-Panah, H. Wang, X. Gong and Y.-C. Yeo, *Opt. Express,* 2019, **27**, 5798–5813.

4 H. Tran, T. Pham, J. Margetis, Y. Zhou, W. Dou, P. C. Grant, J. M. Grant, S. Al-Kabi, G. Sun, R. A. Soref, J. Tolle, Y.-H. Zhang, W. Du, B. Li, M. Mortazavi and S.-Q. Yu, *ACS Photonics*, 2019, **6**, 2807–2815.

5 K.-C. Lee, M.-X. Lin, H. Li, H.-H. Cheng, G. Sun, R. Soref, J. R. Hendrickson, K.-M. Hung, P. Scajev and A. Medvids, *Appl. Phys. Lett.*, 2020, **117**, 012102.

6 M. A. Nawwar, M. S. A. Ghazala, L. M. S. El-Deen and A. E. H. B. Kashyout, *RSC Adv.*, 2022, **12**, 24518.

7 A. Elbaz, D. Buca, N. von den Driesch, K. Pantzas, G. Patriarche, N. Zerounian, E. Herth, X. Checoury, S. Sauvage, I. Sagnes, A. Foti, R. Ossikovski, J.-M. Hartmann, F. Boeuf, Z. Ikonic, P. Boucaud, D. Grützmacher and M. El Kurdi, *Nat. Photonics*, 2020, **14**, 375–382.

8 S. Wirths, R. Geiger, N. von den Driesch, G. Mussler, T. Stoica, S. Mantl, Z. Ikonic, M. Luysberg, S. Chiussi, J. M. Hartmann, H. Sigg, J. Faist, D. Buca and D. Gru¨tzmacher, *Nat. Photonics*, 2015,**9**, 88–92.

9 R. Chen, S. Gupta, Y.-C. Huang, Y. Huo, C. W. Rudy, E. Sanchez, Y. Kim, T. I. Kamins, K. C. Saraswat and J. S. Harris, *Nano Lett.*, 2014, **14**, 37–43.

10 O. Moutanabbir, S. Assali, X. Gong, E. O'Reilly, C. A. Broderick, B. Marzban, J. Witzens, W. Du, S-Q.

Yu, A. Chelnokov, D. Buca and D. Nam, *Appl. Phys. Lett.*, 2021, **118**, 110502.

11 C. Xu, D. Ringwala, D. Wang, L. Liu, C. D. Poweleit, S. L. Y. Chang, H. L. Zhuang, J. Menéndez and J. Kouvetakis, *Chem. Mater.*, 2019, **31**, 9831–9842.

12 D. Rainko, Z. Ikonic, A. Elbaz, N. von den Driesch, D. Stange, E. Herth, P. Boucaud, M. E. Kurdi, D. Grützmacher and D. Buca, *Sci. Rep.*, 2019, **9**, 259.

13 J. Liu, X. Sun, D. Pan, X. Wang, L. C. Kimerling, T. L. Koch and J. Michel, *Opt. Express*, 2007, **15**, 11272–11277.

14 M. K. Hudait, F. Murphy-Armando, D. Saladukha, M. B. Clavel, P. S. Goley, D. Maurya, S. Bhattacharya and T. J. Ochalski, *ACS Appl. Electron. Mater.*, 2021, **3**, 4535–4547.

15 M. Clavel, P. Goley, N. Jain, Y. Zhu and M. K. Hudait, *IEEE J. Electron Devices Soc.*, 2015, **3**, 184–193.

16 T. Liu, L. Wang, G. Zhu, X. Hu, Z. Dong, Z. Zhong, Q. Jia, X. Yang and Z. Jiang, *Semicond. Sci. Technol.*, 2018, **33**, 125022.

17 E. Rogowicz, J. Kopaczek, J. Kutrowska-Girzycka, M. Myronov, R. Kudrawiec and M. Syperek, *ACS Appl. Electron. Mater.*, 2021, **3**, 344–352.

18 E. Gaubas, J. Vanhellemont, E. Simoen, I. Romandic, W. Geens, P. Clauws, *Phys. B (Amsterdam, Neth.)*, 2007, **401–402**, 222–225.

19 S. Gupta, E. Simoen, R. Loo, Y. Shimura, C. Porret, F. Gencarelli, K. Paredis, H. Bender, J. Lauwaert, H. Vrielinck and M. Heyns, *Appl. Phys. Lett.*, 2018, **113**, 022102.

20 D. S. Sukhdeo, S. Gupta, K. C. Saraswat, B. R. Dutt and D. Nam, *Opt. Commun.*, 2016, **364**, 233–237.

21 H. Mączko, R. Kudrawiec and M. Gladysiewicz, *Sci. Rep.,* 2016, **6**, 34082.

22 S. Dominici, H. Wen, F. Bertazzi, M. Goano and E. Bellotti, *Opt. Express*, 2016, **24**, 26363–26381.

23 S. Wirths, Z. Ikonic, A. T. Tiedemann, B. Holländer, T. Stoica, G. Mussler, U. Breuer, J. M. Hartmann, A. Benedetti, S. Chiussi, D. Grützmacher, S. Mantl and D. Buca, *Appl. Phys. Lett.*, 2013, **103**, 192110.

24 Z. Chen, Z. Ikonic, D. Indjin and R. W. Kelsall, *J. Appl. Phys. (Melville, NY, U. S.)*, 2021, **129**, 123102.

25 J. D. Sau and M. L. Cohen, *Phys. Rev. B.,* 2007, **75**, 045208.

26 S. Gupta, B. Vincent, B. Yang, D. Lin, F. Gencarelli, J.-Y. J. Lin, R. Chen, O. Richard, H. Bender, B. Magyari-Köpe, M. Caymax, J. Dekoster, Y. Nishi and K. C. Saraswat, *2012 IEEE Int. Electron Devices Meet.*, IEEE, San Francisco, CA, USA 2012.

27 N. von den Driesch, D. Stange, S. Wirths, G. Mussler, B. Holländer, Z. Ikonic, J. M. Hartmann, T. Stoica, S. Mantl, D. Grützmacher and D. Buca Chem. Mater., 2015, **27**, 4693–4702.

28 E. T. Simola, V. Kiyek, A. Ballabio, V. Schlykow, J. Frigerio, C. Zucchetti, A. D. Iacovo, L. Colace, Y. Yamamoto, G. Capellini, D. Grützmacher, D. Buca and G. Isella, *ACS Photonics*, 2021, **8**, 2166–2173.

29 M. R. M. Atalla, S. Assali, S. Koelling, A. Attiaoui and O. Moutanabbir, *ACS Photonics*, 2022, **9**, 1425–1433.

30 B. Dutt, H. Lin, D. S. Sukhdeo, B. M. Vulovic, S. Gupta, D. Nam, K. C. Saraswat and J. S. Harris, *IEEE J. Sel. Top. Quantum Electron.*, 2013, **19**, 1502706–1502706.

31 M. K. Hudait, S. W. Johnston, M. B. Clavel, S. Bhattacharya, S. Karthikeyan and R. Joshi, *J. Mater. Chem. C*, 2022, **10**, 10530–10540.

32 J. Davies, *The Physics of Low-dimensional Semiconductors: An Introduction*. Cambridge University Press., Cambridge, 1997.

33 M. Chen, Y. Jung, D. Burt, Y. Kim, H. Joo, L. Zhang, S. Assali, O. Moutanabbir, C. S. Tan and D. Nam, *Conference on Lasers and Electro-Optics*, Technical Digest Series (Optica Publishing Group, 2022), San Jose, CA, U.S., 2022.

34 G. Greene-Diniz and M. Grüning, *Phys. Rev. Appl.*, 2018, **10**, 044052-1–044052-16.

35 B. Julsgaard, N. von den Driesch, P. Tidemand-Lichtenberg, C. Pedersen, Z. Ikonic and D. Buca, *Photonics Res.*, 2020, **8**, 788–798.

36 J. Wang and S. Lee, *Sensors,* 2011, **11**, 696–718.

37 N. E. Christensen, *Phys. Rev. B*, 1988, **38**, 12687.

38 C. G. Van de Walle and R. M. Martin, *Phys. Rev. B*, 1987, **35**, 8154.

39 M. B. Clavel, J.-S. Liu, R. J. Bodnar and M. K. Hudait, *ACS Omega*, 2022, **7**, 5946–5953.

40 Y. Zhu, N. Jain, S. Vijayaraghavan, D. K. Mohata, S. Datta, D. Lubyshev, J. M. Fastenau, Amy K. Liu, N. Monsegue and M. K. Hudait, *J. Appl. Phys. (Melville, NY, U.S.)*, 2012, **112**, 094312.

41 M. Bonfanti, E. Grilli, M. Guzzi, M. Virgilio, G. Grosso, D. Chrastina, G. Isella, H. von Känel and A. Neels, *Phys. Rev. B*, 2008, **78**, 041407.

42 P. F. Gomes, F Iikawa, F. Cerdeira, M. Larsson, A. Elfving, G. V. Hansson, W.-X. Ni and P.-O. Holtz, *Appl. Phys. Lett.*, 2007, **91**, 051917.

43 M. B. Clavel, G. Greene-Diniz, M. Grüning, K. T. Henry, M. Kuhn, R. J. Bodnar and M. K. Hudait, *ACS Appl. Electron. Mater.*, 2019, **1**, 2646–2654.
44 W. S. Yoo, H. Harima and M. Yoshimoto, *ECS J. Solid State Sci. Technol.*, 2015, **4**, P356.
45 E. Anastassakis and M. Cardona, *High Pressure in Semiconductor Physics II*; Academic Press: San Diego, CA, 1998, **55**, Ch. 3.
46 M. K. Hudait, M. Meeker, J.-S. Liu, M. B. Clavel, S. Bhattacharya and G. A. Khodaparast, *Opt. Mater.*, 2022, **131**, 112633.
47 G. H. Major, N. Fairley, P. M. A. Sherwood, M. R. Linford, J. Terry, V. Fernandez and K. Artyushkova, *J. Vac. Sci. Technol., A*, 2020, **38**, 061203.
48 G. Greczynski and L. Hultman, *J. Appl. Phys. (Melville, NY, U.S.)*, 2022, **132**, 011101.
49 X. Jin, S. Chen, T. Li, *Commun Mater.*, 2022, **3**, 66.
50 J. E. Castle, *Practical surface analysis by Auger and X-ray photoelectron spectroscopy*, John Wiley and Sons Ltd, Chichester, 1983.
51 E. A. Kraut, R. W. Grant, J. R. Waldrop and S. P. Kowalczyk, *Phys. Rev. Lett.*, 1980, **44**, 1620−1623.
52 S. Sant and A. Schenk, *Appl. Phys. Lett.*, 2014, **105**, 162101.
53 V. Swaminathan and A. T. MacRander, in *Materials Aspects of GaAs and InP Based Structures*, Prentice Hall, Englewood Cliffs, NJ, U.S., 1991, Ch. 1.
54 M. A. Nawwar, M. S. A. Ghazala, L. M. S. El-Deen, A. El-Shaer, Badawi Anis and A. E. H. B. Kashyout, *Cryst. Growth Des.*, 2023, **23**, 751.
55 C.-Y. Peng, C.-F. Huang, Y.-C. Fu, Y.-H. Yang, C.-Y. Lai, S.-T. Chang, and C. W. Liu, *J. Appl. Phys.*, 2009, **105**, 083537.
56 J. H. Parker, Jr., D. W. Feldman, and M. Ashkin, *Phys. Rev.*, 1967, **155**, 712.
57 S. Su, W. Wang, B. Cheng, W. Hu, G. Zhang, C. Xue, Y. Zuo and Q. Wang, *Solid State Commun.*, 2011, **151**, 647-650.
58 C. Chang, H. Li, T.-P. Chen, W.-K Tseng, H. Cheng, C.-T. Ko, C.-Y. Hsieh, M.-J. Chen, and G. Sun, *Thin Solid Films*, 2015, **593**, 40-43.
59 A. Gassenq, L. Milord, J. Aubin, N. Pauc, K. Guilloy, J. Rothman, D. Rouchon, A. Chelnokov, J. M. Hartmann, V. Reboud, and V. Calvo, *Appl. Phys. Lett.*, 2017, **110**, 112101.
60 T. Schmidt, K. Lischka and W. Zulehner, *Phys. Rev. B: Condens. Matter Mater. Phys.*, 1992, **45**, 8989.
61 T.-H. Cheng, C.-Y. Ko, C.-Y. Chen, K.-L. Peng, G.-L. Luo, C. W. Liu and H.-H. Tseng, *Appl. Phys. Lett.*, 2010, **96**, 091105.
62 G. Grzybowski, R. Roucka, J. Mathews, L. Jiang, R. T. Beeler, J. Kouvetakis, J. Menendez, *Phys. Rev. B: Condens. Matter Mater. Phys.*, 2011, **84**, 205307.
63 S. Gupta, R. Chen, Y.-C. Huang, Y. Kim, E. Sanchez, J. S. Harris and K. C. Saraswat, *Nano Lett.*, 2013, **13**, 3783.
64 J. F. Moulder and J. Chastain, *Handbook of X-Ray Photoelectron Spectroscopy : A Reference Book of Standard Spectra for Identification and Interpretation of Xps Data*, Perkin-Elmer Corp Physical Electronics Division, Eden Prairie, Minnesota, U.S., 1992.
65 National Center for Biotechnology Information, PubChem Periodic Table of Elements, https://pubchem.ncbi.nlm.nih.gov/periodic-table/, (accessed Nov. 2022).
66 E. T. Yu, J. O. McCaldin and T. C. McGill, in *Solid State Physics*, California Institute of Technology, Pasadena, California U.S., 1992, Band Offsets in Semiconductor Heterojunctions, 1–146.
67 M. Peressi, N. Binggeli and A. Baldereschi, *J. Phys. D: Appl. Phys.*, 1998, **31**, 1273.
68 W. A. Harrison, E. A. Kraut, J. R. Waldrop and R. W. Grant, *Phys. Rev. B*, 1978, **18**, 4402.
69 L. J. Brillson, in *Surfaces and Interfaces of Electronic Materials*, Wiley: Weinheim, 2010, Ch. 20.
70 M.B. Clavel, F. Murphy-Armando, Y. Xie, K.T. Henry, M. Kuhn, R.J. Bodnar, G.A. Khodaparast, D. Smirnov, J.J. Heremans and M.K. Hudait, *Phys. Rev. Appl.*, 2022, **18**, 064083.
71 N. Pavarelli, T. J. Ochalski, F. Murphy-Armando, Y. Huo, M. Schmidt, G. Huyet and J. S. Harris, *Phys. Rev. Lett.*, 2013, **110**, 177404.
72 D. Stange, N. von den Driesch, D. Rainko, C. Schulte-Braucks, S. Wirths, G. Mussler, A. T. Tiedemann, T. Stoica, J. M. Hartmann, Z. Ikonic, S. Mantl, D. Grützmacher and D. Buca, *Opt. Express*, 2016, **24**, 1358–1367.
73 S. A. Ghetmiri, *Si-based Germanium-Tin (GeSn) Emitters for Short-Wave Infrared Optoelectronics*, University of Arkansas, Fayetteville, 2016.
74 H. S. Mączko, R. Kudrawiec and M. Gladysiewicz, *Sci. Rep.*, 2016, **6**, 34082.
75 N. von den Driesch, D. Stange, D. Rainko, I. Povstugar, P. Zaumseil, G. Capellini, T. Schröder, T. Denneulin, Z. Ikonic, J.-M. Hartmann, H. Sigg, S. Mantl, D. Grützmacher and D. Buca, *Adv. Sci. (Weinheim, Ger.)*, 2018, **5**, 1700955.
76 H. Zhou, S. Xu, Y. Lin, Y.-C. Huang, B. Son, Q.

Chen, X. Guo, K. H. Lee, S. C.-K. Goh, X. Gong and C. S. Tan, *Opt. Express*, 2020, **28**, 10280–10293.

77 H. Wang, J. Zhang, G. Zhang, Y. Chen, K. Han, Y.-C. Huang and X. Gong, *IEEE Trans. Electron Devices*, 2022, **69**, 2166–2172.